

Numerical Simulation of a Single-Wafer Isothermal Plasma Etching Reactor

Sang-Kyu Park and Demetre J. Economou*

Department of Chemical Engineering, University of Houston, Houston, Texas 77204-4792

ABSTRACT

A two-dimensional finite element simulation of gas flow and reactive species distribution in a parallel-plate single-wafer isothermal reactor was conducted. The oxygen plasma etching of polymer under high pressure (~1 torr), high frequency (13.56 MHz) conditions was chosen as a model system for analysis with emphasis on chemical etching. Etching rate and uniformity were examined as a function of reactor geometry and operating conditions. A maximum in etching rate with flow rate was observed, and this maximum shifted to higher flow rates as the power increased. The pressure dependence of the etching rate was complex, but in general a broad maximum in etching rate with pressure existed, which shifted to higher pressures as the flow rate increased. Etching rate increased but etching uniformity degraded as the wafer reactivity increased. A shower radius at least equal to the wafer radius, and a plasma radius slightly greater than the wafer radius were found to give the best etching rate and uniformity results under the conditions examined. Two novel reactor designs were also studied, namely, a reactor with a graded gas velocity at the shower, and a pulsed-plasma reactor. When compared to the conventional reactor, the new designs can yield improved uniformity and etching rate (the etching rate of the pulsed-plasma reactor was prorated by the duty cycle).

Plasma-assisted etching and deposition of thin films using reactive gas glow discharges is currently in widespread use in the microelectronics industry (1). However, despite the importance of plasma processing, reactive gas glow discharges are not well understood. This may be due to the nonequilibrium nature of the plasma, and the complex interaction among potential field, transport phenomena, plasma chemistry, and surface reaction kinetics. Thus, the fact that plasma reactor design is still based largely on empirical approaches is not surprising. Recently, there has been an increased interest in developing mathematical models of the plasma process in an effort to better understand the process, and to assist in the rational design of plasma reactors (2-10). The modeling studies have been complemented by a host of plasma diagnostic techniques (11-13).

Important requirements of plasma-assisted etching include high etching rate, uniformity, anisotropy, and selectivity, and no radiation damage. However, as is often the case in complex engineering systems, it is very difficult to satisfy all of the above requirements simultaneously. For example, one may desire to operate at relatively high pressure in order to increase the etching rate. Nevertheless, under such condition one may have to sacrifice uniformity, because of low reactant diffusivity, and/or anisotropy because of low ion bombardment energy. Therefore, "optimum" parameter settings may be identified for which the etching rate, for instance, is maximized while uniformity and anisotropy are within acceptable limits.

As the wafer size continues to increase and stringent requirements are placed on reaction uniformity, the use of single-wafer reactors becomes increasingly compelling. In addition to improved uniformity, other advantages of single-wafer etchers, as compared to multi-wafer batch systems, are better process control and reproducibility. Although single-wafer etching reactors are used extensively in the semiconductor industry, there are very few published works on the transport and reaction phenomena occurring in such reactors.

A mathematical model for a single-wafer etcher was recently developed (2). Given information on reaction kinetics, the model predicted etching rate, uniformity, and anisotropy. Emphasis was placed on the effect of reactor operating conditions on etching uniformity. The oxygen plasma system was selected to test the model predictions. An experimental technique based on optical emission actinometry and the Abel transform was developed to obtain the three-dimensional etchant concentration profile. Experimental data were in good quantitative agreement with the model predictions over a wide range of operating conditions. The encouraging results of this earlier work

prompted the authors to carry out a more detailed investigation of the single-wafer etcher.

In the present work, an extension of the previous mathematical model is presented. Specifically, a more practical reactor configuration was considered including part of the etching chamber downstream from the plasma region, and separate mass balances for the etchant species and for the parent gas molecules were written. The finite element method was used to calculate the fluid velocity distribution and in turn the concentration distribution of active species. A similar model was very recently reported by Kobayashi *et al.* (6) for the etching of aluminum. In the present work, the oxygen plasma etching of polymer was used as a model system because pertinent reaction constants are known, and because the electron density and energy can be estimated as a function of reactor geometry and operating parameters. The effect of reactor design on the etching rate and uniformity was studied assuming that chemical etching was the dominant mechanism (negligible ion-assisted etching). The effect of flow rate, pressure, power, etching rate constant, and radius of electrode, wafer, and shower was studied. Two novel reactor designs were also examined, namely, a reactor with a graded gas flow velocity at the showerhead, and a pulsed-plasma reactor.

Mathematical Model Formulation

The model was developed for the single-wafer etcher shown schematically in Fig. 1. The axisymmetric reactor has a showerhead upper electrode and a lower electrode where the wafer rests. Feedstock gas enters through the shower of the showerhead electrode and is pumped radially towards the reactor exit. The plasma was assumed to be confined between the equal area electrodes, and the gas temperature was assumed to be spatially uniform. Furthermore, the wafer was assumed to be in good thermal contact with the temperature-controlled lower electrode.

The reactor dimensions are shown in Fig. 2 where, owing to symmetry, only half of the reactor is shown. The two electrodes were assumed to have the same radius, r_2 . However, the wafer radius r_1 , as well as the shower radius r_3 of the showerhead electrode could be smaller than the electrode radius. Radii r_1 , r_2 , and r_3 were varied. Other reactor dimensions were kept constant at the values shown in Fig. 2. Basic parameter values used for calculations and the range of parameter values examined are shown in Table I. Other parameter values are shown in Table II.

As with any plasma etching reactor, modeling of the single-wafer etcher requires consideration of the plasma physical chemistry, the ion transport in the sheath, and the transport and reaction phenomena of important species and of heat in both the plasma region and the "downstream" region. The present investigation emphasizes ap-

* Electrochemical Society Active Member.

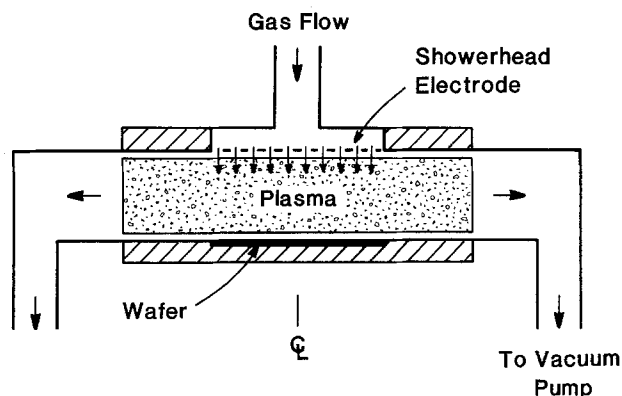


Fig. 1. Schematic of the parallel-plate single-wafer etching reactor studied.

lications for which ion-assisted etching is of secondary importance. Hence, ion transport in the sheath was not considered. In the case of polymer etching in an oxygen discharge examined here, appropriate conditions for chemical etching to dominate would be relatively high pressure (~1 torr) and high excitation frequency (>10 MHz). Furthermore, a simplified treatment of the gas discharge was adopted, as was done in previous work (2, 3). Specifically, the effective electric field E_{ef} approximation was used, and the ratio E_{ef}/p was found as a function of $p\Lambda$, where p is the gas pressure and Λ is the electron diffusion length given by

$$\frac{1}{\Lambda^2} = \left(\frac{2.405}{r_2}\right)^2 + \left(\frac{\pi}{H}\right)^2 \quad [1]$$

In addition, a Maxwellian electron energy distribution function was assumed with an electron temperature which is a unique function of E_{ef}/p . The average electron density in the plasma region n_e was found by

$$\frac{P}{v_p} = \frac{n_e e^2 E_{ef}^2}{m v_e} \quad [2]$$

where P is the power dissipated in the plasma, v_p is the plasma volume ($v_p = \pi H r_2^2$), e and m are the electron charge and mass, respectively, and v_e is the electron momentum transfer collision frequency. An electron density equal to zero was assumed outside the plasma. An important assumption was that the discharge is not significantly affected by the etching reaction products, i.e., the discharge was treated as if it were one in pure oxygen. This assumption is better for low etching rate and high gas flow rate, conditions which minimize the concentration of reaction products. The advantages of the above treatment of

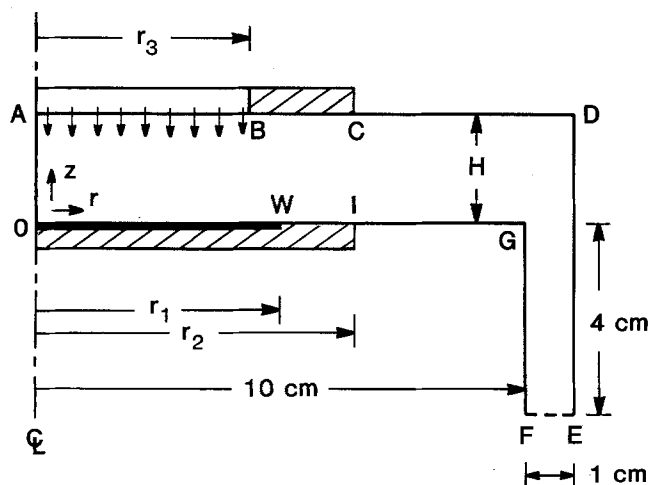


Fig. 2. Dimensions of the single-wafer etching reactor considered; r_1 , r_2 , and r_3 were varied.

Table I. Parameter values used for calculations

Symbol	Name	Basic value	Range examined
k_p	Etching rate constant	50 cm/s	10-100 cm/s
P	Plasma power	100W	25-200W
p	Gas pressure	1 torr	0.5-2 torr
Q	Inlet gas flow rate	100 sccm	10-500 sccm
r_1	Wafer radius	5 cm	1-6.5 cm
r_2	Electrode radius	6.5 cm	5-8 cm
r_3	Shower radius	6.5 cm	1-8 cm

Table II. Other parameter values

Symbol	Name	Value
H	Interelectrode spacing	2.2 cm
f	Plasma pulsing frequency	100 Hz
T	Gas temperature	298 K
k_1	Volume recombination rate constant	$4.782 \cdot 10^{14} \text{ cm}^6/\text{mol}^2\text{-s}$
k_2	Volume recombination rate constant	$8.343 \cdot 10^{14} \text{ cm}^6/\text{mol}^2\text{-s}$
k_3	Volume recombination rate constant	$5.441 \cdot 10^{13} \text{ cm}^6/\text{mol}^2\text{-s}$
γ	Wall recombination coefficient	$1.6 \cdot 10^{-4}$

the discharge are simplicity of calculation and account of the variation of electron energy and density with reactor geometry and operating conditions. The disadvantages of the above treatment are that the model is not applicable in the low-pressure, low-frequency regime where secondary electron emission effects may be important, the electron energy distribution function (which may well be non Maxwellian) is not found, and any effects of the etching reaction products on the plasma chemistry are not considered. Nevertheless, use of the simplified discharge model has been previously met with success (2, 3).

With the electron temperature T_e known, the rate constant of reactions involving electrons may be calculated. For example, the rate constant k_p of the electron impact dissociation reaction [R1], may be found using Eq. [3] below, where $\sigma_p(\epsilon)$ is the reaction cross section as a function of electron energy ϵ , and k is the Boltzmann constant



$$k_p = \sqrt{\frac{8}{\pi m}} (kT_e)^{-3/2} \int_0^\infty \epsilon \sigma_p(\epsilon) \exp\left(-\frac{\epsilon}{kT_e}\right) d\epsilon \quad [3]$$

Fluid velocity distribution.—Under the conditions examined, the pressure is high enough for the continuum approximation to be valid, and the flow is isothermal, laminar, and axisymmetric. Moreover, neglecting any change in the number of moles due to reaction, the momentum balance equations can be decoupled from the mass balance equations. The velocity field was obtained by solving the steady-state Navier-Stokes equations

$$\rho \mathbf{v} \cdot \nabla \mathbf{v} = \nabla \cdot \boldsymbol{\tau} + \rho \mathbf{g} \quad [4]$$

where the tensor

$$\boldsymbol{\tau} = -p\mathbf{I} + \mu [\nabla \mathbf{v} + (\nabla \mathbf{v})^T] \quad [5]$$

\mathbf{I} being the identity matrix, along with the continuity equation

$$\nabla \cdot \mathbf{v} = 0 \quad [6]$$

Here $\mathbf{v} = (U, W)$ is the fluid velocity vector, U is the radial velocity, W is the axial velocity, and ρ and μ are the fluid density and viscosity, respectively. The following boundary conditions were applied on fluid velocity, where the boundary condition (BC) number refers to the corresponding surface as shown in Fig. 3

$$\text{BC1} \quad \frac{\partial W}{\partial n} = 0 \quad U = 0 \quad [7]$$

$$\text{BC2 } U = 0 \quad W = -W_w \quad [8]$$

$$\text{BC3, 4, 6-9 } U = W = 0 \quad [9]$$

$$\text{BC5 } \frac{\partial W}{\partial n} = 0 \quad U = 0 \quad [10]$$

Here n is the unit normal pointing outwards the computational domain, and W_w is the gas velocity at the shower of the showerhead electrode (reactor inlet velocity). Three cases were examined: (i) a uniform gas velocity at the shower

$$W_w = \frac{Q}{\pi r_3^2} \quad [11]$$

Q being the feedstock gas volumetric flow rate at plasma reactor conditions, (ii) a gas velocity which was zero at the shower center $r = 0$, and which increased linearly with radial position to its maximum value at the shower edge $r = r_3$

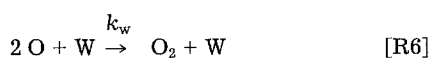
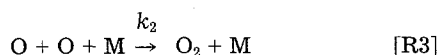
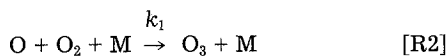
$$W_w = \frac{2Qr}{\pi r_3^3} \quad [12]$$

and (iii) a gas inlet velocity which was maximum at the shower center and which decreased to zero at the shower edge

$$W_w = \frac{2Q}{\pi r_3^3} (r_3 - r) \quad [13]$$

BC1 is a symmetry condition along the reactor centerline, BC2 is the boundary condition at the shower (along segment AB in Fig. 2), BC5 implies a fully developed gas flow at the reactor exit, and BC3, BC4, BC6-BC9 are the no-slip condition at solid surfaces.

Mass transport and reaction.—A variety of neutral and charged species in both the ground and excited states may be found in the oxygen discharge (14-16). Important neutral species are molecular and atomic oxygen and perhaps metastable oxygen and ozone. However, molecular oxygen at the ground state is the dominant gas-phase species. Atomic oxygen has been found to be the main etchant in relatively high pressure oxygen plasma etching of photoresist (17, 18). In order to simplify the analysis, only three neutral species were considered, namely, molecular oxygen, atomic oxygen, and etching reaction product. Atomic oxygen is produced in the plasma mainly by electron-impact dissociation of molecular oxygen (19) according to reaction [R1]. The corresponding reaction rate is $r_p = 2k_p n_e C_2$, where C_2 is the concentration of molecular oxygen. Etchant production takes place in the plasma region only. The rate constant k_p is given by Eq. [3]. Atomic oxygen is consumed by volume recombination reactions [R2]-[R4], by the etching reaction [R5], and by wall recombination reaction [R6] (14)



Here k_1 , k_2 , k_3 are the volume recombination rate constants, k_n is the etching reaction rate constant, and k_w is the

wall recombination rate constant. M is a third body required to conserve both energy and momentum during collision, S is the polymer surface where etching occurs, W represents a wall, and P represents the etching reaction product. Constants k_1 , k_2 , and k_3 were obtained from the literature (14). Volume recombination reactions are strongly pressure dependent and are normally insignificant at pressures less than about 1 torr. In this work M was assumed to be O_2 , the dominant gas-phase species. The etching reaction rate constant was assigned a basic value of $k_n = 50$ cm/s. However, the effect of changing the value of k_n was examined. Constant k_w was written as

$$k_w = \frac{1}{4} \gamma u_o \quad [14]$$

where γ is the wall recombination coefficient, and u_o is the thermal velocity of the oxygen atoms given by

$$u_o = \sqrt{\frac{8kT}{\pi M_1}} \quad [15]$$

where M_1 is the oxygen-atom mass and T is the gas temperature. The value of the wall recombination coefficient was assumed to be $\gamma = 1.6 \cdot 10^{-4}$ (20).

Mass balance equations were written for both molecular and atomic oxygen, neglecting multicomponent diffusion effects and using a pseudo-binary diffusion coefficient

$$\frac{\partial C_i}{\partial t} + \mathbf{v} \cdot \nabla C_i = \nabla \cdot (CD_i \nabla x_i) + G_i \quad [16]$$

where C is the total gas concentration ($C = p/R_g T$), and C_i , x_i , D_i , and G_i are molar concentration, mole fraction, diffusivity, and net production rate of species i , respectively. Subscripts $i = 1$ and $i = 2$ refer to atomic and molecular oxygen, respectively. The net volumetric production rate of atomic oxygen was written as

$$G_1 = 2k_p(t) n_e(t) C_2 - (k_1 C_1 C_2^2 + 2k_2 C_1^2 C_2 + 2k_3 C_1^3) \quad [17]$$

and that of molecular oxygen was written as

$$G_2 = -k_p(t) n_e(t) C_2 - k_1 C_1 C_2^2 + (k_2 C_1^2 C_2 + k_3 C_1^3) \quad [18]$$

The first term on the right-hand side (rhs) of Eq. [17] is the production of O atoms according to reaction [R1]. The corresponding rate constant and the electron density are a function of time in the case of pulsed-plasma reactor considered later. The first, second, and third terms in parenthesis on the rhs of Eq. [17] correspond to O-atom elimination according to reactions [R2], [R3], and [R4], respectively. Despite the fact that the production of etchant is localized in space and occurs in the discharge region only, etchant volume recombination occurs throughout the reactor volume. The mass balance for the reaction product P was not considered since its mole fraction can be found from the other two species mole fractions and the fact that the mole fractions must sum up to unity. The O-O₂ binary diffusion coefficient was estimated from experimental collision diameter data (21), and the O₂ self-diffusion coefficient was estimated using standard techniques (22). Etching and wall recombination reactions enter in the boundary conditions for Eq. [16] which are described below

$$\text{BC1 } \frac{\partial x_i}{\partial n} = 0 \quad [19]$$

$$\text{BC2 } D_1 C \frac{\partial x_1}{\partial n} = W_w [C_{1o} - C_1] \quad [20]$$

$$\text{BC3, 4, 6-8 } \begin{cases} D_1 C \frac{\partial x_1}{\partial n} = -k_w C_1 & [21] \\ D_2 C \frac{\partial x_2}{\partial n} = \frac{1}{2} k_w C_1 & [22] \end{cases}$$

$$\text{BC5} \quad \frac{\partial x_1}{\partial n} = 0 \quad [23]$$

$$\text{BC9} \quad D_1 C \frac{\partial x_1}{\partial n} = -k_n C_1 \quad [24]$$

where C_{i0} is the species concentration in the feedstock gas ($i = 1, 2$), and n is along the surface normal pointing outwards the computational domain. Equations [20] and [23] are Danckwerts-type boundary conditions (34) at the reactor entrance and exit, respectively. Equations [21] and [22] represent wall recombination on all surfaces other than the wafer surface. Linear wall recombination kinetics was assumed (20). Equation [24] represents etching at the wafer surface. Only chemical etching was considered, and simple linear kinetics was assumed (17, 23).

Before proceeding any further, the model assumptions are summarized below. (i) The discharge was treated as if it were one in pure oxygen, *i.e.*, product interference was neglected. (ii) Only neutral chemistry was considered, and atomic oxygen was taken to be the only etchant species of photoresist. (iii) Ion bombardment effects were neglected. (iv) Linear etching and wall recombination reactions were assumed. (v) The electron energy distribution function was assumed Maxwellian. (vi) The continuum approximation was made, and the gas was assumed to be a Newtonian incompressible fluid with constant physical properties (density, viscosity). (vii) Multicomponent transport effects were neglected and a constant diffusivity was used. (viii) The plasma was assumed to be confined between the electrodes, and the gas and wafer temperatures were assumed spatially uniform. In addition, for the case of pulsed-plasma reactor, the following three assumptions were made. (ix) The flow field was assumed unaffected by pulsing of the plasma. (x) The effective rate constant for etchant production $k_{\text{eff}} = k_p n_e$ (see Eq. [17]) was assumed to be completely modulated by the applied waveform (a square wave modulation). (xi) During the power-on fraction of the cycle, a 13.56 MHz excitation frequency was applied.

Method of Solution

The finite element method was used to solve the governing equations (24, 25). The computational domain and the finite element mesh used for most calculations are shown in Fig. 3. Owing to symmetry, only half of the reactor was considered. Figure 3 refers to the base case corresponding to the parameter values shown in the third column of Table I (*i.e.*, $r_2 = r_3 = 6.5$ cm, and $r_1 = 5$ cm). The momentum balance and the mass balance equations were solved separately. Such decoupling of the equations is permissible in isothermal systems in which there is negligible change in the number of moles upon reaction. In the present case, the approximation is better at low power and pressure and high flow rate, conditions which result in small degree of dissociation of the parent gas. The decoupling of the equations resulted in substantial savings in computation time.

The continuity and momentum balance Eq. [4]-[6] along with the associated boundary conditions Eq. [7]-[10] were

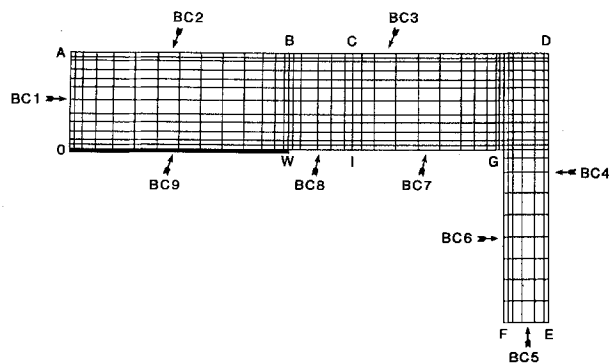


Fig. 3. Finite element mesh used for most calculations. BC number indicates the surface on which the corresponding boundary condition was applied.

solved first. The penalty function formulation (26, 27) was employed to eliminate pressure as one of the dependent variables. The penalty parameter was selected as $10^8 \mu$ (27). The convective diffusion Eq. [16] subject to boundary conditions Eq. [19]-[24] were solved next using the known velocity field. The streamline upwind Petrov-Galerkin finite element method (28, 29) was used with bilinear basis functions. The resulting set of nonlinear algebraic equations was solved using the skyline solver of gauss elimination (24). For all the results reported below the steady-state form of Eq. [16] was solved, except for the pulsed-plasma reactor.

For the pulsed-plasma reactor, it was assumed that the flow field is not affected by the pulse, and therefore the steady-state fluid velocity distribution was used. The finite element discretization of the convective diffusion Eq. [16] led to a set of ordinary differential equations of the form

$$\dot{\mathbf{M}}\mathbf{C} + \mathbf{N}(\mathbf{C}) = \mathbf{F} \quad [25]$$

where $\dot{\mathbf{C}}$ is the temporal derivative of vector $\mathbf{C} = (C_1, C_2)$, \mathbf{M} is the mass matrix, $\mathbf{N}(\mathbf{C})$ is a nonlinear vector-valued function, and \mathbf{F} is the force vector. A predictor/multi-corrector scheme with generalized trapezoidal method was employed to solve Eq. [25] (24). The following error norm was used to detect the periodic steady-state solution

$$\epsilon_{\text{pss}} = \left\{ \frac{\sum_{j=1}^{N_R} \left[\left(\frac{R_j}{R_{\text{av}}} \right)_{(i+1)T_p} - \left(\frac{R_j}{R_{\text{av}}} \right)_{iT_p} \right]^2}{N_R^2} \right\}^{1/2} \quad [26]$$

where ϵ_{pss} is a user-specified error tolerance, N_R is the number of nodes along the wafer radius (typically 15), R_i is the etching rate at node i , R_{av} is the average etching rate, I is an integer counter, and T_p is the pulse period. The number of pulse periods (and hence the computation time) required to achieve the periodic steady-state depended critically on the gas flow rate, and it was typically several hundred (using $\epsilon_{\text{pss}} = 10^{-6}$) for low flow rates (*e.g.*, 20 sccm) decreasing at higher flow rates. The time integration step was chosen ten times smaller than the pulse period.

Results and Discussion

The effect of the parameters shown in Table I on etching rate and uniformity was studied. Basic parameter values are shown in the third column of Table I. The range of parameter values examined is shown in the fourth column of the same table. Parameter values shown in Table II were kept constant. In order to study the effect of a parameter, the value of that parameter was varied while keeping the other parameters at their basic value. In the following calculations all parameters were at their basic value unless noted otherwise.

Figure 4 is a velocity vector plot. The vectors show the magnitude and direction of the local fluid velocity. The axial velocity component has its maximum value at the reactor entrance ($r = 0.0$ -6.5 cm, $z = 2.2$ cm) and decreases monotonically to become zero at the wafer surface. The ra-

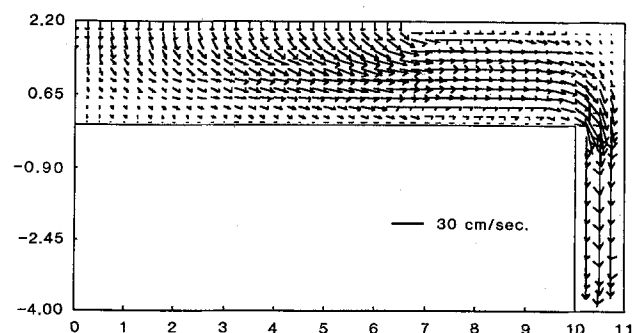


Fig. 4. Fluid velocity vector plot. Parameters were at their basic value.

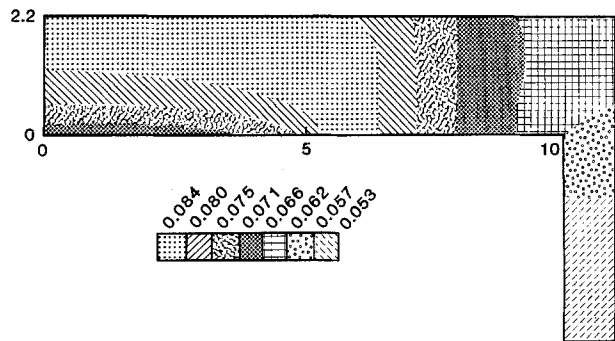


Fig. 5. Concentration distribution of atomic oxygen (mole fraction). Parameters were at their basic value.

dial velocity component is zero at the reactor center and increases linearly with radius up to $r = r_3 = 6.5$ cm. Beyond the shower edge and up to the reactor corner region (around $r = 10$ cm) the velocity profile is nearly parabolic with a zero axial component. Approximate analytic expressions for the velocity distribution in the plasma region were given before (2).

Figure 5 shows the etchant (O-atom) mole fraction distribution. The mole fraction varies between 5.3 and 8.4% under the conditions of Fig. 5. Since the wafer is a sink of etchant species, the etchant concentration decreases as the wafer surface is approached. In addition, a significant etchant concentration gradient exists along the wafer radius. This radial concentration gradient is more pronounced around the periphery of the wafer ($r = 5$ cm) where a reactive surface (wafer) and a relatively inert surface (electrode) meet. This is due to etchant diffusing from the plasma volume above the relatively inert electrode to react on the wafer. Since the etching rate is a monotonic function of etchant concentration, such gradient would result in nonuniform etching. In fact, the situation depicted in Fig. 5 would result in a "bullseye" film clearing pattern in which the film clears at the wafer edges first. Beyond the plasma region (the plasma radius was 6.5 cm), there is no more etchant production, and the etchant concentration decreases monotonically due to volume and wall recombination reactions. Etching nonuniformity was extensively studied in a previous work (2).

Figure 6 shows the atomic oxygen concentration as a function of radial position along the wafer surface, for dif-

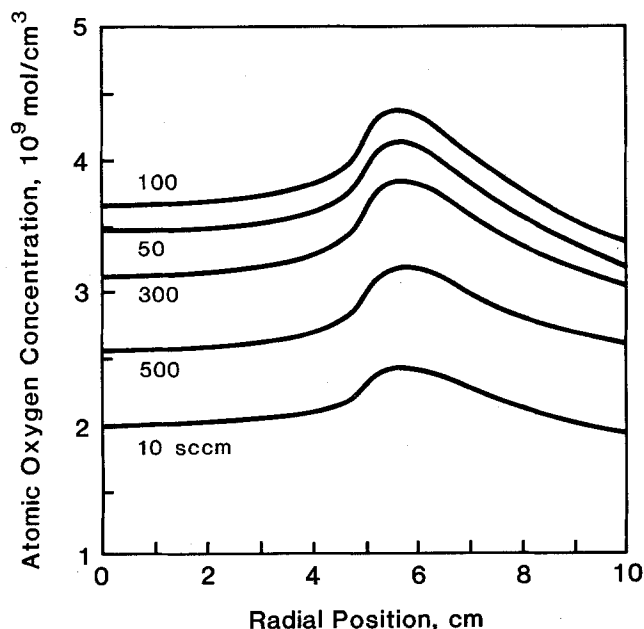


Fig. 6. Atomic oxygen concentration as a function of radial position along the substrate electrode for different gas flow rates. Other parameters were at their basic value.

ferent values of the gas flow rate. Other parameters were at their basic value. One observes large concentration gradients around the periphery of the wafer ($r = 5$ cm) and around the plasma edge ($r = 6.5$ cm), and the concentration reaches a maximum between these two locations. The maximum in concentration can be clearly seen in Fig. 5 as well. Moreover, since the etching rate was assumed proportional to the etchant concentration (Eq. [29] below), the etching rate profiles will be identical to the concentration profiles shown in Fig. 6. The spatially averaged etchant concentration first increases with flow rate, reaches a maximum, and then decreases monotonically with flow rate. The flow rate effect is examined in more detail below (Fig. 7).

The etching rate R was calculated by

$$R(\text{A/min}) = CF R(\text{mol O/cm}^2\text{-s}) \quad [27]$$

where the conversion factor CF is given by

$$CF = \frac{1}{q} \left(\frac{MW_f}{\rho_f} \right) \left(\frac{60}{10^{-8}} \right) \quad [28]$$

and $R(\text{mol O/cm}^2\text{-s})$ is given by

$$R = k_n C_1 \quad [29]$$

Here C_1 is the local O-atom concentration, q is the number of moles of atomic oxygen consumed by one mole of the monomeric unit of the polymer (photoresist) film, ρ_f and MW_f are the film density and molecular weight of the monomer, respectively. The values used were $q = 11$, $\rho_f = 1.28 \text{ g/cm}^3$, $MW_f = 94$. These values correspond to etching of a Novolac-type photoresist represented by the formula $(C_6H_6O)_n$ assuming that half of the carbon is converted to CO_2 and the other half to CO (30). The above parameter values are arbitrary but reasonable, and are used here simply to give an idea of what the etching rate in a single-wafer reactor may be under the conditions examined. The average etching rate was calculated from the local etching rate by using

$$R_{av} = \frac{2}{r_1^2} \int_0^{r_1} R r dr \quad [30]$$

Figure 7 shows the average etching rate as a function of the flow rate for different values of power. At low flow rates etching is limited by reactant supply, and at high flow rates etching is limited by convective removal of the reactant. Hence, a maximum etching rate exists. The maximum shifts slowly to higher flow rate as the power increases. One further observes that the etching rate is not as sensitive to flow rate at very high flow rates. The etching

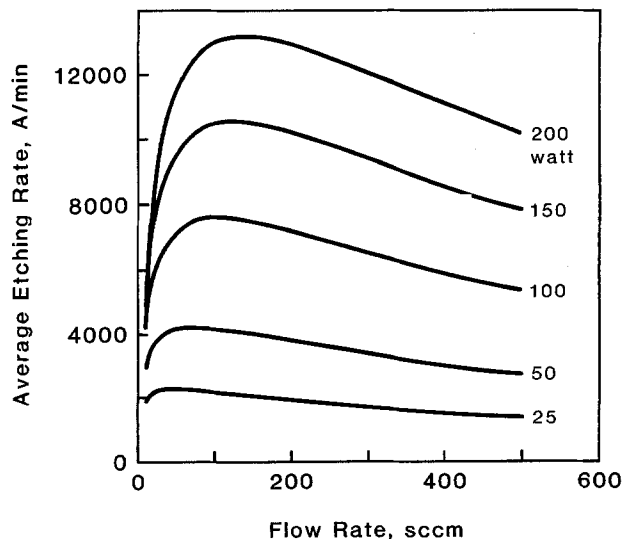


Fig. 7. Average etching rate as a function of gas flow rate for different values of power. Other parameters were at their basic value.

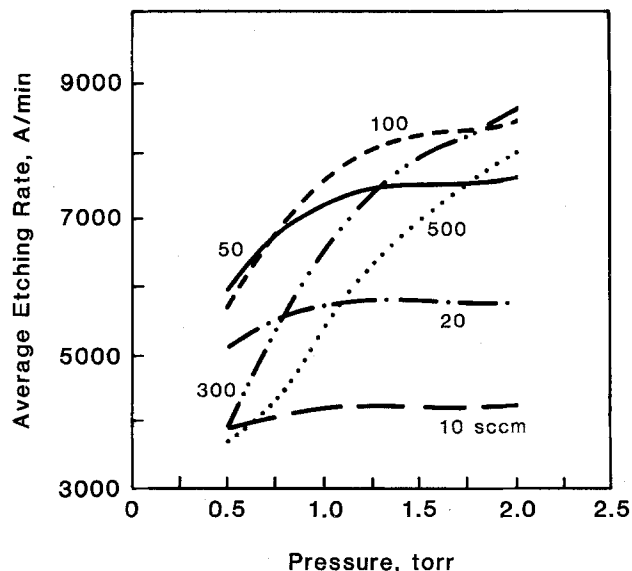


Fig. 8. Average etching rate as a function of pressure for different gas flow rates. Other parameters were at their basic value.

rate was found to increase almost linearly with power at low power values. This was the result of electron density increasing linearly with power. However, the power dependence of etching rate turned into sublinear at higher power values, especially at high pressure.

The effect of pressure is shown in Fig. 8. Over the pressure range examined, the etching rate is relatively insensitive to pressure at low flow rate, but increases rapidly with pressure at high flow rate. At very high pressure, the etching rate is expected to fall because volume recombination reactions become very important, and because the electron energy decreases with pressure resulting in lower dissociation rate. For a given flow rate, the pressure dependence of the etching rate appears to exhibit a broad maximum, and this maximum shifts to higher pressure as the flow rate increases. Similar behavior has been found in a plasma-assisted downstream etching reactor (31). Figure 8 also shows that for a given pressure, there is a flow rate which maximizes the etching rate. This flow rate is pressure dependent. For example, at 1 torr, the maximum etching rate is obtained at around 100 sccm (see also Fig. 7).

The local etching rate as a function of radius along the wafer is shown in Fig. 9, with the chemical etching rate

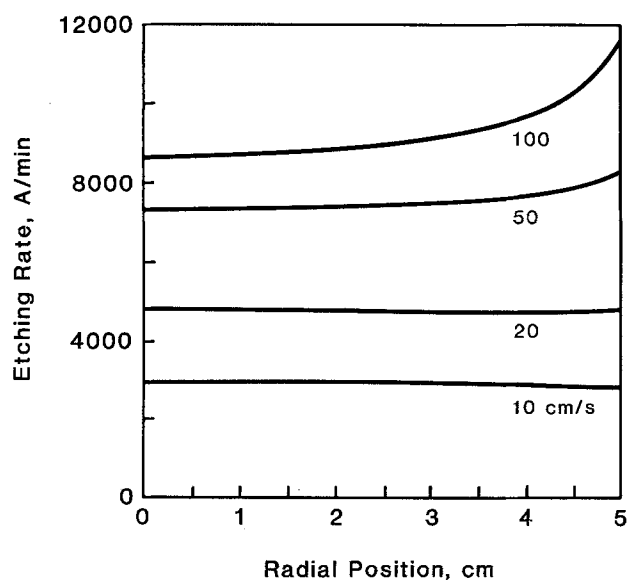


Fig. 9. Etching rate as a function of radial position along the wafer for different values of the chemical etching reaction rate constant. Other parameters were at their basic value.

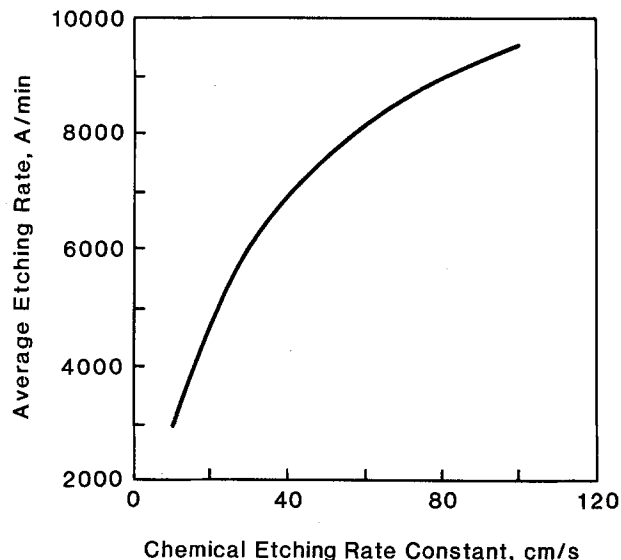


Fig. 10. Average etching rate as a function of the chemical etching reaction rate constant. Other parameters were at their basic value.

constant k_n as a parameter. Etching is fairly uniform when the reactivity of the wafer is low (small k_n). Under such condition, diffusion is rapid enough to replenish the reactant consumed on the wafer surface. This is not the case, however, when etching is rapid (large k_n), resulting in non-uniform etching. The value of k_n above which etching becomes nonuniform depends on the reactivity of the electrode surrounding the wafer (2). The etching rate increases with k_n , as seen in Fig. 10, despite the fact that the etchant concentration decreases with k_n (not shown here). As the chemical etching rate constant increases, the relative gain in etching rate diminishes. For very large values of k_n , the etching rate will be diffusion controlled, and hence insensitive to the value of k_n .

Figure 11 shows the etching rate along the wafer radius for different radii of the gas shower of the showerhead electrode, r_3 . The pressure and the total flow rate Q were kept constant at their basic value of 1 torr and 100 sccm, respectively, and therefore the nominal residence time ($\tau = pv_p/Q$) is independent of r_3 . Nevertheless, both etching rate and uniformity depend on r_3 . For small values of r_3 , etching is highly nonuniform. Let us examine the case of $r_3 = 1$ cm as an example, remembering that the wafer radius was 5 cm and that the plasma radius was 6.5 cm. Beyond

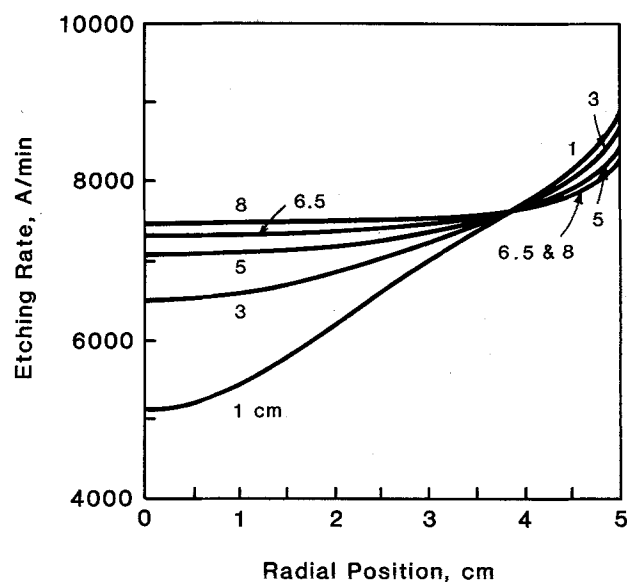


Fig. 11. Etching rate as a function of radial position along the wafer for different values of the shower radius of the showerhead electrode. Other parameters were at their basic value.

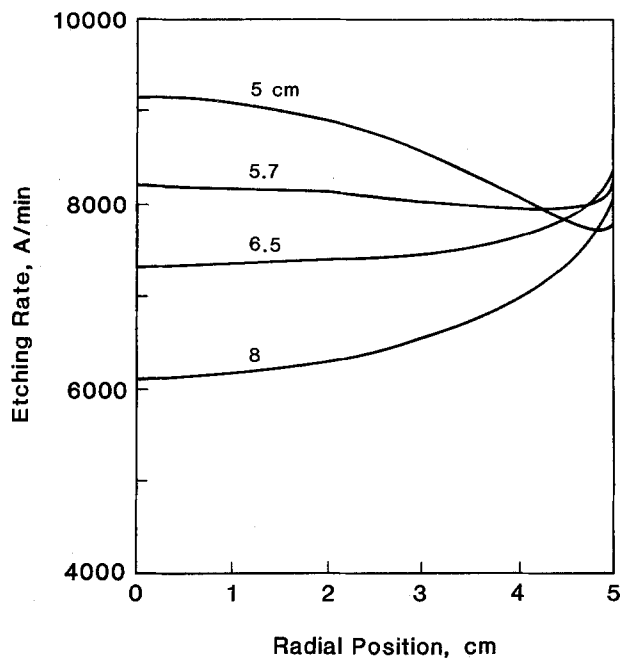


Fig. 12. Etching rate as a function of radial position along the wafer for different values of the electrode (and plasma) radius. Other parameters were at their basic value.

the radius of 1 cm, the gas decelerates (velocity inversely proportional to radius) with a concomitant increase of the gas residence time in the plasma. This leads to increased dissociation as the gas flows radially outwards, and in turn to an etching rate increasing with radius. As the shower radius increases, the gas residence time distribution is altered such that etching uniformity improves monotonically. Figure 11 shows that the details of the residence time distribution are important in determining the etching rate and uniformity in plasma reactors. Further examination of Fig. 11 shows that the shower radius must be at least equal to the wafer radius to avoid excessive etching nonuniformity.

The effect of electrode (and plasma) radius r_2 is shown in Fig. 12. The wafer radius was 5 cm, and the gas was uniformly distributed over the entire showerhead electrode surface (i.e., $r_2 = r_3$, see Fig. 2). Other parameters were at their basic value. As the electrode radius decreases, the power density in the plasma increases (power was kept constant), and this results in higher etching rate. For a plasma radius significantly greater than the wafer radius, etchant species generated beyond the wafer radius contribute to etching, yielding higher etching rate around the wafer periphery as compared to the wafer center (case of 6.5 cm and 8 cm electrode radius in Fig. 12). However, for plasma radius equal to the wafer radius (case of 5 cm), the etching profile changes dramatically. In such case, the etching rate decreases monotonically from the wafer center to the wafer periphery. Production of etchant species now occurs only over the wafer, and etchant diffusion away from the plasma results in lower concentration around the wafer periphery. The situation would be even worse for plasma radii smaller than the wafer radius. Etching can be made nearly uniform by using an electrode radius slightly larger than the wafer radius as shown in Fig. 12, for the case of an electrode with 5.7 cm radius.

Figure 13 shows the etching rate along the wafer radius for different wafer radii r_1 . Other parameters were at their basic value. As the wafer radius (wafer area) decreases, etching rate increases. This is the so-called loading effect, and appears when the etching reaction is an important etchant loss mechanism. Etching nonuniformity increases as well with decreasing wafer radius. Moreover, for wafer radii less than the plasma radius (the latter was 6.5 cm), the typical bullseye wafer clearing pattern would be observed. However, for wafer radius equal to the plasma radius, the reverse clearing pattern would be observed. This observation is similar to that of Fig. 12 for the case of equal wafer

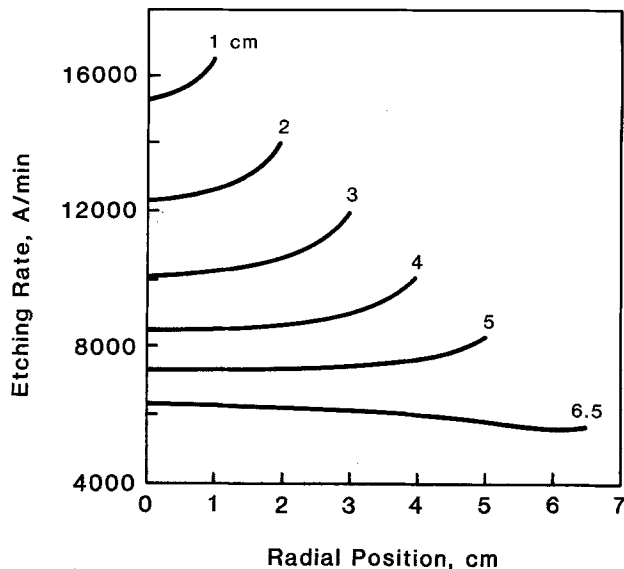


Fig. 13. Etching rate as a function of radial position along the wafer for different values of wafer radius. Other parameters were at their basic value.

and plasma radii (5 cm in that case). The loading effect is further shown in Fig. 14 where the inverse of the average etching rate is plotted as a function of the square of the wafer radius (proportional to wafer area) (32). The squares are calculated points and the solid line is a fit to guide the eye. A nearly linear plot is obtained. The plot would have been strictly linear if concentrations were spatially uniform, if volume recombination reactions were neglected, and if the molecular oxygen mole fraction remained constant as the wafer radius changed. The behavior shown in Fig. 13 and 14 may be expected in the absence of reaction product interference. For example, if a product of the etching reaction participates in other reactions which produce etchant species, an inverse loading effect may be found, i.e., the etching rate may increase with increasing wafer area (35).

An advantage of mathematical modeling is that reactor design alternatives may be evaluated rapidly, before any costly experimentation. Promising designs may then be chosen for further examination including experimental verification of the model. In this context, the usefulness of the present mathematical model will be demonstrated by

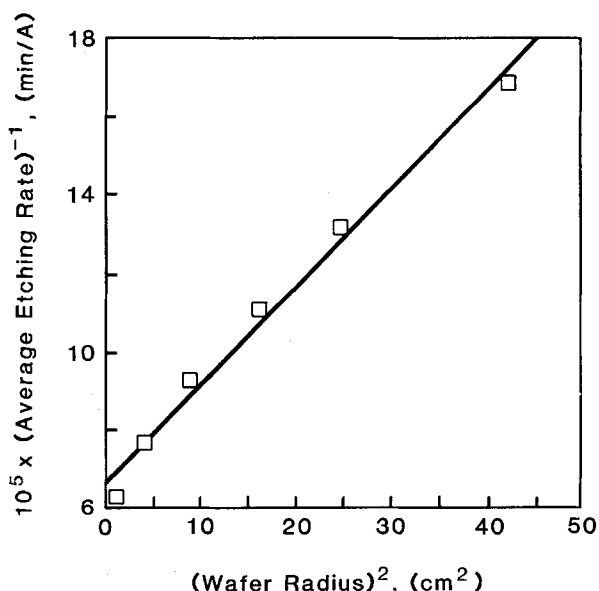


Fig. 14. Inverse average etching rate as a function of the square of wafer radius (proportional to wafer area). Other parameters were at their basic value.

studying two novel reactor designs, namely, a reactor with a graded velocity profile at the shower, and a pulsed-plasma reactor.

Plasma reactor with a graded inlet velocity profile.—Figure 15 shows the etching rate along the wafer radius for three different gas velocity profiles at the shower. Parameters were at their basic value, except that the gas flow rate was 500 sccm. Case A corresponds to the basic reactor design of uniform shower velocity (Eq. [11]). Case B corresponds to a shower velocity which increases linearly from the center to the edge of the shower (Eq. [12]). One observes an improvement in etching uniformity by using the graded profile. This can be explained as follows: the typical situation is one in which the reactant concentration increases monotonically from the center to the edge of the wafer. Compared to the basic case, the graded velocity profile results in increased residence time close to the reactor center (increasing the chance for gas dissociation), and in faster etchant removal from the wafer edge. The final result is a milder etchant concentration gradient. The opposite is true for a shower velocity profile which is maximum at the center and decreases to zero at the shower edge (Eq. [13]). The latter case (curve C in Fig. 15), yields worse uniformity as compared to the basic case. It is conceivable that the etching rate can be made nearly uniform by choosing the appropriate flow rate. Alternatively, for a given flow rate, a velocity profile may be found (not necessarily linear) which would yield nearly uniform etching. Figure 15 also reveals that the etching rate is higher with the graded velocity profile (case B), as compared to the conventional case of uniform velocity profile (case A). The result in Fig. 15 further demonstrates that the details of the gas residence time distribution are important in determining the etching rate and uniformity. For example, in all three cases of Fig. 15 the nominal gas residence time was the same, yet different results were obtained for each case.

Pulsed-plasma etching reactor.—Another example of novel reactor design is that of a pulsed-plasma etching reactor (PPER). In the PPER to be examined, the plasma is modulated at a frequency much lower than the common radio frequencies. For instance, consider the case shown in Fig. 16. A square power waveform is applied with a frequency of 100 Hz and a duty cycle of 50%. During the 5 ms of power-on, the plasma may be operated at the usual frequency of 13.56 MHz in order to achieve higher efficiency of gas dissociation and to avoid intense ion bombardment and/or charging of insulating surfaces. Although more

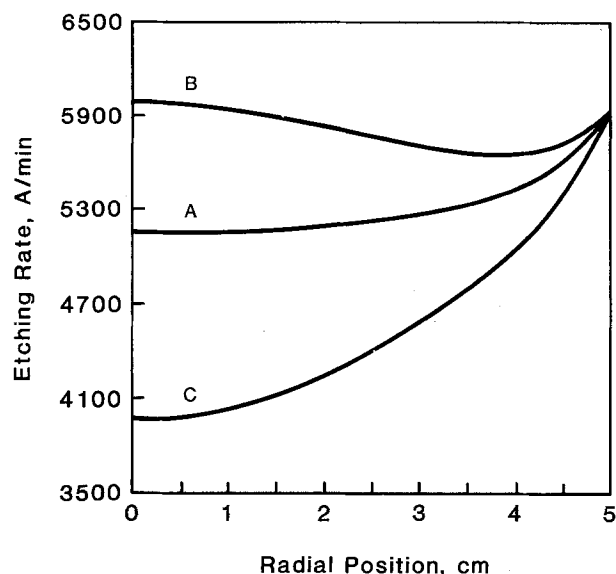


Fig. 15. Etching rate as a function of radial position along the wafer for different gas velocity profiles at the shower. A, velocity profile given by Eq. [11]; B, velocity profile given by Eq. [12]; C, velocity profile given by Eq. [13]. Parameters were at their basic value except that the gas flow rate was 500 sccm.

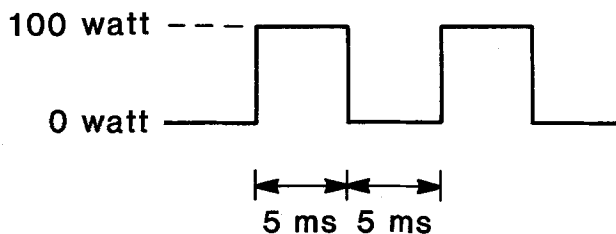


Fig. 16. Power waveform considered for pulsed-plasma reactor. During the 5 ms power-on fraction of the period the plasma was operated at a frequency of 13.56 MHz.

complex situations can arise (33), it was assumed that the electron density and energy were modulated according to the applied power waveform. Therefore, the effective etchant production rate constant $k_{eff} = k_p n_e$ was assumed to follow exactly the applied waveform shown in Fig. 16. Despite the fact that the plasma may be completely modulated by the applied power waveform, the response of the species concentration depends on the modulation frequency, the gas residence time, and the species reaction time.

Figure 17 shows the space-time dependence of the etching rate for the case of plasma modulation shown in Fig. 16. Other parameters were at their basic value except that the flow rate was 20 sccm. The plot of Fig. 17 corresponds to the periodic steady-state achieved after a number of cycles. The etching rate increases with time during the power-on portion of the cycle, reaches a maximum, and then decreases monotonically during the power-off portion of the cycle. The decay time depends on the time scale for etchant loss by gas flow and by reactions such as etching, and wall and volume recombination. For a period of modulation which is long relative to the decay time (low modulation frequency), the etching rate would be very small throughout most of the power-off portion of the cycle. At the opposite extreme of high modulation frequency, the etching rate would be nearly time independent.

The dependence of the space- and time-average etching rate on gas flow rate is shown in Fig. 18 for the basic plasma reactor design [continuous-wave (cw) reactor, curve A; see also Fig. 7 for $P = 100W$] and the PPER (curve B). As before, the plasma was modulated according to the waveform shown in Fig. 16. One observes a similar behavior with flow rate for both the cw and pulsed-plasma reactors, i.e., the etching rate passes through a maximum. For high flow rates, for which the pulse period is much larger than the gas residence time, the etching rate in the PPER is that of the cw reactor prorated by the duty cycle.

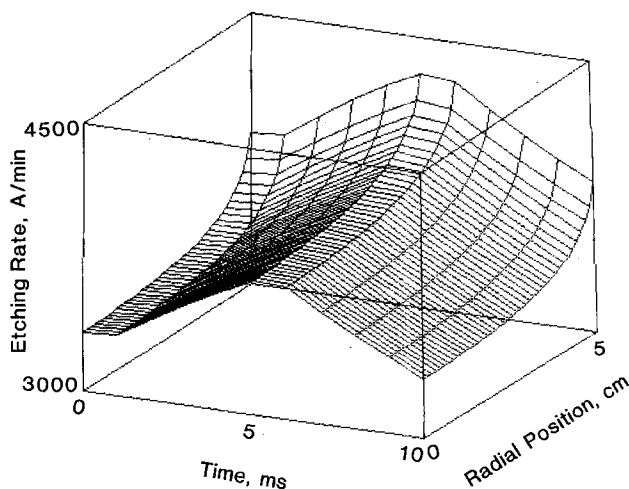


Fig. 17. Space-time evolution of the etching rate along the wafer radius for a pulsed-plasma reactor. This plot corresponds to the periodic steady-state achieved after a number of cycles. Applied power waveform as in Fig. 16. Parameters were at their basic value except that the gas flow rate was 20 sccm.

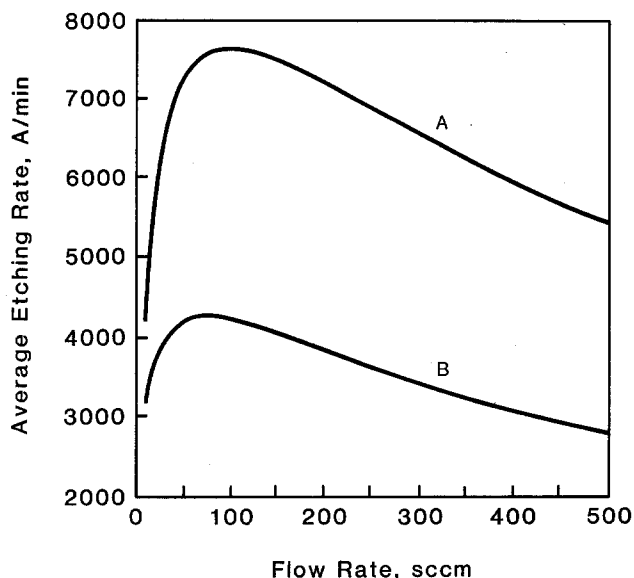


Fig. 18. Space- and time-averaged etching rate as a function of gas flow rate. A, continuous-wave (cw) plasma reactor; B, pulsed-plasma reactor. Applied power waveform as in Fig. 16. Other parameters were at their basic value.

In the case of Fig. 18, the PPER rate is 50% of the cw reactor rate for high flow rates. However, for low flow rates, the etching rate in the PPER is higher than the cw reactor rate prorated by the duty cycle. For example, at 20 sccm, the etching rate with the cw reactor prorated by the duty cycle is 2850 A/min. However, the rate achieved using the PPER is 3700 A/min.

Figure 19 shows that another advantage of the pulsed-plasma reactor is better etching uniformity as compared to the cw plasma reactor. The higher the reactor pressure, the greater the improvement in uniformity when using the pulsed-plasma reactor. A disadvantage of PPER is that during the power-off fraction of the cycle etching is due to neutral species only. This may result in degradation of etching anisotropy. A detailed analysis of a pulsed-plasma reactor will be presented elsewhere (36).

Summary and Conclusions

A two-dimensional mathematical model for a parallel-plate isothermal single-wafer plasma etching reactor was developed. The etching chamber analyzed included both the plasma region and part of the downstream region. The oxygen plasma etching of polymer was chosen as a model system for analysis. The finite element method was employed to calculate the fluid velocity profiles and the concentration distribution of reactive species. Emphasis was placed on conditions for which chemical etching was the dominant mechanism (negligible ion-assisted etching). Etching rate and uniformity were studied as a function of reactor geometry and operating conditions. The range of operating conditions studied was pressure 0.5-2 torr, power 25-200W, and flow rate 10-500 sccm.

For given reactor pressure, a maximum etching rate with gas flow rate was observed. The maximum shifted to higher gas flow rates with increasing power. The pressure dependence of the etching rate was rather complex. At low flow rates (e.g., <20 sccm), the etching rate was relatively insensitive to pressure over the pressure range examined. At higher flow rates, the etching rate as a function of pressure seemed to exhibit a broad maximum, with the maximum shifting to higher pressures as the flow rate increased.

As the etching reaction rate constant (wafer reactivity) increased ($k_n = 10-100$ cm/s), the etching rate increased but the etching uniformity degraded. The etching uniformity improved as the wafer reactivity became comparable to the reactivity of the surrounding electrode surface. The etching uniformity was also affected by the shower radius of the showerhead electrode and by the plasma radius. Uniformity was low for small shower radii and improved monotonically by increasing the shower radius. A shower radius at least equal to the wafer radius is recommended to avoid excessive nonuniformity. Uniformity of etching as a function of the plasma radius was examined for plasma radii equal to or larger than the wafer radius. A plasma radius slightly larger than the wafer radius (e.g., 15% larger) was found to give the best results under the conditions examined.

Two novel reactor designs were studied in an effort to improve reactor performance. A graded velocity at the shower (instead of a constant velocity) resulted in improvements in both etching rate and uniformity. A pulsed-plasma reactor can result in improved uniformity and

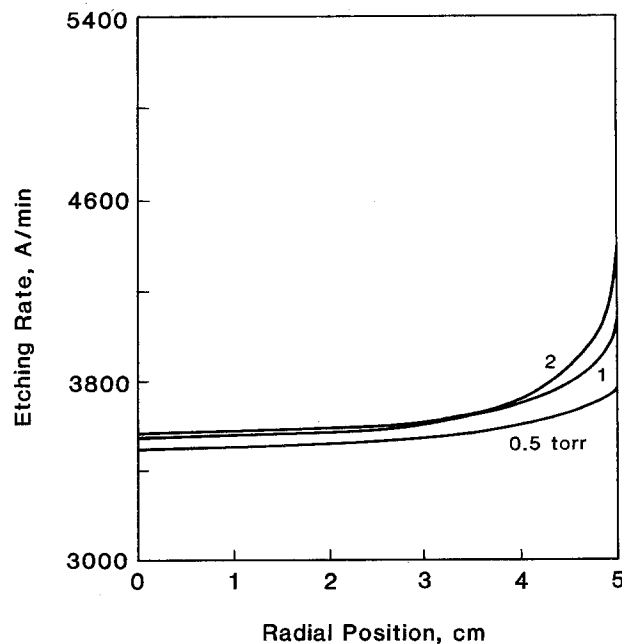
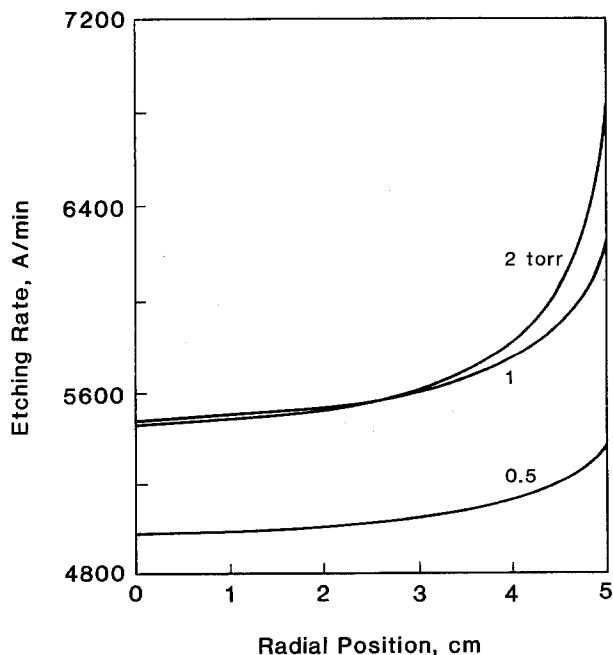


Fig. 19. (a, left) Etching rate as a function of radial position along the wafer for the continuous-wave reactor. (b, right) Time-averaged etching rate as a function of radial position along the wafer for the pulsed-plasma reactor. For (b), applied power waveform was as in Fig. 16. For both (a) and (b) parameters were at their basic value except that the gas flow rate was 20 sccm.

higher etching rate (when etching rate is prorated by the duty cycle) as compared to a continuous-wave plasma reactor.

Neglecting the effect of the reaction products on the discharge chemistry and physics is thought to be the most critical assumption of the present model. Hence, the model results will be more accurate under conditions of negligible product interference. An example is low power and high flow rate for which the product concentration is minimized.

Plasma reactor systems are characterized by complex physics and chemistry, and current understanding of reactive gas plasmas is incomplete. Even if all reaction channels and the corresponding rate constants were known, the state-of-the-art supercomputers are not sufficiently powerful to solve the equations of a model which includes details of all important plasma reactor phenomena. Plasma reactor engineering models based on transport and reaction principles and tested with experimental observations can be valuable reactor design tools. The power of such models will improve tremendously when they are integrated with models of discharge physics and chemistry.

Acknowledgments

This work was supported by the National Science Foundation (CBT-8708908). We are grateful to the Houston Area Research Center (HARC) for an SX-2 supercomputer time grant. S.-K. Park was partially supported by a scholarship from the Ministry of Education, Republic of Korea.

Manuscript submitted Aug. 15, 1989; revised manuscript received Jan. 15, 1990.

The University of Houston assisted in meeting the publication costs of this article.

LIST OF SYMBOLS

C	total gas concentration, moles/cm ³
C_i	concentration of species i , moles/cm ³
C_{i0}	inlet concentration of species i , moles/cm ³
CF	conversion factor (Eq. [28])
D_i	diffusion coefficient of species i , cm ² /s
E_{ef}	effective electric field, V/cm
F	force vector (Eq. [25])
e	electronic charge, 1.602 10 ⁻¹⁹ C
f	plasma pulsing frequency, s ⁻¹
G_i	net production rate of species i , moles/cm ³ -s
H	interelectrode spacing, cm
k	Boltzmann constant, 1.38066 10 ⁻²³ J/K
k_1, k_2, k_3	volume recombination rate constants, cm ⁶ /mol ² -s
k_n	chemical etching rate constant, cm/s
k_p	etchant production rate constant, cm ³ /s
k_w	wall recombination rate constant, cm/s
M	mass matrix (Eq. [25])
M	third body (Eq. [R2] and [R3])
M_1	atomic oxygen mass, g
MW_f	molecular weight of photoresist, g/mole
m	electronic mass, 9.1095 10 ⁻²⁸ g
N	vector-valued function (Eq. [25])
N_R	number of nodes along wafer radius (Eq. [26])
n_e	electronic density, cm ⁻³
P	power, W; reaction product (Eq. [R5])
p	pressure, dynes/cm ²
Q	gas flow rate, cm ³ /s
q	number of moles of atomic oxygen reacting with a monomeric unit of the photoresist film (Eq. [28])
R	etching rate, moles/cm ² -s or A/min
R_{av}	average etching rate, A/min
R_g	gas constant, 62,358 torr-cm ³ /mole-K
R_j	etching rate at node j , A/min
r	radial coordinate, cm
r_1	electrode radius, cm
r_2	wafer radius, cm
r_3	shower radius, cm
S	signifies the etching surface (Eq. [R5])
T	gas temperature, K
T_e	electron temperature, K
T_p	pulse period, s
t	time, s
U	radial gas velocity, cm/s

u_o	thermal velocity of oxygen atoms, cm/s
v	fluid velocity vector
v_p	plasma volume, cm ³
W	axial gas velocity, cm/s; wall (Eq. [R6])
W_w	gas velocity at shower, cm/s
x_i	mole fraction of species i
z	axial coordinate, cm

Greek

γ	wall recombination coefficient
ϵ	electron energy, eV
ϵ_{ps}	error tolerance for detection of periodic steady state
Λ	electron diffusion length, cm
μ	gas viscosity, g/cm-s
ν_e	electron momentum transfer collision frequency, s ⁻¹
ρ	gas density, g/cm ³
ρ_f	photoresist film density, g/cm ³
σ_p	electron-impact dissociation cross section, cm ²

REFERENCES

1. "VLSI Electronics: Microstructure Science," Vol. 8, "Plasma Processing for VLSI," N. G. Einspruch and D. M. Brown, Editors, Academic Press, Inc., New York (1984).
2. D. J. Economou, S.-K. Park, and G. D. Williams, *This Journal*, **136**, 188 (1989).
3. D. J. Economou and R. C. Alkire, *ibid.*, **135**, 2786 (1988).
4. I. C. Plumb and K. R. Ryan, *Plasma Chem. Plasma Process.*, **6**, 205 (1986); *ibid.*, **6**, 231 (1986).
5. D. Edelson and D. Flamm, *J. Appl. Phys.*, **56**, 1522 (1984).
6. J. Kobayashi, N. Nakazato, and K. Hiratsuka, *This Journal*, **136**, 1781 (1989).
7. G. Rogoff, J. Kramer, and R. Piejak, *IEEE Trans. Plasma Sci.*, **PS-14**, 103 (1986).
8. E. Zawaideh and N. S. Kim, *J. Appl. Phys.*, **64**, 4199 (1988).
9. K. D. Allen, H. H. Sawin, M. T. Mocella, and M. W. Jenkins, *This Journal*, **133**, 2315 (1986); K. D. Allen and H. H. Sawin, *ibid.*, **133**, 2326 (1986); K. D. Allen, H. H. Sawin, and A. Yokozeki, *ibid.*, **133**, 2331 (1986).
10. R. Gottscho, A. Mitchell, G. Scheller, N. Schryer, D. Graves, and J.-P. Boeuf, "Plasma Processing," (PV 88-22) G. S. Mathad and D. W. Hess, Editors, p. 1, The Electrochemical Society Softbound Proceedings Series, Pennington, NJ (1989).
11. V. M. Donnelly, D. L. Flamm, and R. H. Bruce, *J. Appl. Phys.*, **58**, 2135 (1986).
12. R. Gottscho and T. Miller, *Pure Appl. Chem.*, **56**, 189 (1984).
13. R. W. Dreyfus, J. M. Jasinski, R. E. Walkup, and G. S. Selwyn, *ibid.*, **57**, 1265 (1985).
14. A. T. Bell, in "Techniques and Applications of Plasma Chemistry," J. R. Hollahan and A. T. Bell, Editors, John Wiley & Sons, Inc., New York (1974).
15. J. W. Dettmer, Ph.D. Thesis, AFIT/DS/78-3, Air Force Institute of Technology (1978).
16. H. Sabadil and S. Pfau, *Plasma Chem. Plasma Process.*, **5**, 67 (1985).
17. J. M. Cook and B. W. Benson, *This Journal*, **130**, 2459 (1983).
18. M. A. Hartney, D. W. Hess, and D. S. Soane, *J. Vac. Sci. Technol.*, **B7**, 1 (1989).
19. F. Kaufman, in "Chemical Reactions in Electrical Discharges," Advances in Chemistry Series, Vol. 80, p. 29, ACS, Washington, DC (1969).
20. J. C. Graves and J. W. Linnett, *Trans. Faraday Soc.*, **55**, 1355 (1959).
21. R. A. Young, *J. Chem. Phys.*, **34**, 1295 (1961).
22. R. C. Reid, J. M. Prausnitz, and T. K. Shewood, "The Properties of Gases and Liquids," 3rd. ed., McGraw Hill Inc., New York (1977).
23. J. F. Battey, *This Journal*, **124**, 147 (1977); *IEEE Trans. Electron. Devices*, **ED-24**, 140 (1977).
24. T. J. R. Hughes, "The Finite Element Method: Linear Static and Dynamic Finite Element Analysis," Prentice-Hall, Inc., Englewood Cliffs, NJ (1987).
25. O. C. Zienkiewicz, "The Finite Element Method," 3rd ed., McGraw Hill, Inc., New York (1977).
26. T. J. R. Hughes, W. K. Liu, and A. Brooks, *J. Comp. Phys.*, **30**, 1 (1979).
27. J. N. Reddy, *Int. J. Num. Meth. Fluids*, **2**, 151 (1982).
28. A. Brooks and T. J. R. Hughes, *Comp. Meth. Appl.*

- Mech. Eng.*, **32**, 199 (1982).
 29. T. E. Tezduyar and D. K. Ganjoo, *ibid.*, **59**, 49 (1986).
 30. R. F. Reichelderfer, J. M. Welty, and J. F. Battey, *This Journal*, **124**, 1926 (1977).
 31. S.-K. Park and D. J. Economou, *J. Appl. Phys.*, **66**, 3256 (1989).
 32. C. J. Mogab, *This Journal*, **124**, 1262 (1977).
 33. L. J. Overzet, J. T. Verdeyen, R. M. Roth, and F. F. Carasco, *Mater. Res. Soc. Sym. Proc.*, **98**, 321 (1987).
 34. P. V. Danckwerts, *Chem. Eng. Sci.*, **2**, 1 (1953).
 35. N. R. Lerner and T. Wydeven, *This Journal*, **136**, 1426 (1989).
 36. S.-K. Park and D. J. Economou, *This Journal*, **137**, 2103 (1990).

Characterization of Silicon Surface Contamination and Near-Surface Damage Caused by C₂F₆/CHF₃ Reactive Ion Etching

Sun Jin Yun, Seong-Ju Park, and Mun-Cheol Paek

Electronics & Telecommunications Research Institute, Daejeon 305-606, Korea

Jeong Y. Lee

Korea Institute of Technology, Daejeon 305-701, Korea

ABSTRACT

Silicon surface contamination and near-surface damage of the Si(100) substrate caused by reactive ion etching (RIE) of SiO₂ overlayer in C₂F₆/CHF₃ plasma were characterized by x-ray photoelectron spectroscopy (XPS), He-ion channeling technique and high-resolution transmission electron microscopy (HRTEM). XPS study indicates that a thin (<20Å thick) C,F polymeric layer was formed on the Si surface and underneath the polymer film a thin oxide layer (~10Å) was produced due to air exposure after RIE. These films were also characterized in terms of chemical composition and bonding states. The C,F film displays six bonding states of carbon, i.e., CF₃, CF₂, CF, C—CF_x, C—C—H, and C—Si. The variations of etchant gas composition and overetching time represent that the content of fluorine in residue film increase with increasing CHF₃ gas fraction and overetching time. The formation of residue film on SiO₂ surface were also investigated. The residue deposited on SiO₂ surface is thinner and contains less concentration of fluorine than the residue on Si surface. He ion scattering/channeling spectrum and cross-sectional high resolution transmission electron micrograph showed that the damaged layer contains displaced Si of about 1 × 10¹⁶ atom/cm², and about 25Å thick amorphous layer is present on the crystalline silicon substrate. In the micrograph of the 2 min overetched sample, point defect clusters or small isolated amorphized region and distorted lattice spacing were found in the near surface region of silicon within 200Å depth.

Patterning by anisotropic dry etching technique is a necessary step for fabrication of very large scale integrated (VLSI) devices and reactive ion etching (RIE) has become the standard process to achieve anisotropic etching (1-3). The RIE anisotropy is mostly based on energetic ion bombardments to the surface of a film to be etched, and a direct exposure to reactive plasmas can lead to bombardment damage (4-7) and also deposition of involatile fluorocarbon film (8-16). The ion-induced damage and the residue deposition are more severe, as overetching time increases. In practical application, overetching is necessary to ensure a complete removal of the film due to nonuniformity in etch rate or a film thickness across a large wafer. The surface residue and the crystalline damage introduced by energetic ion bombardment during overetching would affect device properties and performances, and a series of post-RIE treatments is highly desirable to proceed with further device fabrication (16, 17). In order to develop a suitable post-RIE residue cleaning and damage annealing processes, it is necessary to understand the physical and chemical nature of polymer residues and ion-induced damage in Si.

In this work, Si and SiO₂ specimens previously exposed to RIE mode C₂F₆/CHF₃ plasmas were characterized by x-ray photoelectron spectroscopy (XPS), He-ion channeling technique (RBS), and high resolution transmission electron microscopy (HRTEM). A mixture of C₂F₆ and CHF₃ has been widely used to selectively etching the oxide over Si, since they provide fluorine to generate volatile SiF₄, and carbon to remove oxygen as CO_x. Our objective of the present work is to quantitatively analyze the surface residue and damage introduced by C₂F₆/CHF₃ RIE process, using XPS, RBS, and HRTEM. The residue on the Si surface was also compared with that on the SiO₂ surface.

Experimental

The (100) p-type Si substrates with 3000Å thick thermally grown oxide film were used in order to simulate the

real SiO₂ etching situation and subsequent overetching on the Si surface.

Reactive ion etching experiments were performed in QUAD 484, Drytek RIE system using a C₂F₆/CHF₃ gas mixture. Etching conditions are RF power density of 1.215 W/cm² and the self-induced bias voltage -80V, the total gas flow of 50 sccm, and the chamber pressure of 250 mtorr. The etch rate of SiO₂ was about 1500 Å/min at 50% C₂F₆/50% CHF₃. The end point was determined by a change in the dc bias voltage, as it reaches the interface. In the study of the residue on SiO₂ surface, a SiO₂ film on Si substrate was exposed for 2 min under the same etching condition as described above and then the surface of SiO₂ overlayer partially remained after RIE process was analyzed by XPS. This was confirmed by the elemental Si 2p peak which was not detected on the remained SiO₂ layer. For the study of Si surface residue, the Si substrates remained in the plasma for 2 and 5 min after the end-point detection. The plasma gas composition, C₂F₆/CHF₃, was varied with the mixing ratios of 30%/70%, 50%/50%, 70%/30%, at the conditions of total gas flow 50 sccm and 2 min overetching. After removal from the RIE chamber, the etched specimens were studied without further treatment in the as-etched and air-exposed states.

X-ray photoelectron spectra were obtained with Perkin-Elmer PHI 5400 ESCA instrument using Mg K_α (1253.6 eV) x-ray source. Survey spectra were recorded with 89.45 eV pass energy and narrow scan spectra of all regions of interest were recorded with 71.55 eV pass energy. The fine structures of narrow scan spectra were resolved to characteristic component peaks by a least squares fitting technique using gaussian and lorentzian functions. The backgrounds were nonlinearly subtracted by the integrated method (18, 19). Angle-resolved profiles were obtained by rotating the sample surface, i.e., varying the take-off angle.

The RBS were performed with the NEC 35DH RBS instrument. A 2.275 MeV He ion beam was aligned to the <100> axis of the Si sample. The data were obtained with a